Finite-Difference Computation of Transient Electromagnetic Waves for Cylindrical Geometries in Complex Media

Fernando L. Teixeira and Weng Cho Chew, *Fellow, IEEE*

***Abstract*—We present two novel, fully three-dimensional (3-D) finite-difference time-domain (FDTD) schemes in cylindrical coordinates for transient simulation of electromagnetic wave propagation in complex (inhomogeneous, dispersive, and conductive) and unbounded media. The proposed FDTD schemes incorporate an extension of the perfectly matched layer (PML) absorbing boundary condition (ABC) to three-dimensional (3-D) cylindrical coordinates. Dispersion on the media is modeled by using the piecewise-linear recursive convolution (PLRC) algorithm, accounting for multiterm Lorentz and/or Debye models. Split-field and unsplit (anisotropic medium) formulations of the cylindrical PML-PLRC-FDTD schemes are implemented and compared in the time domain. The comparison includes the late-time stability properties of the update schemes. Numerical simulations of susbsurface electromagnetic problems are included. Because the proposed schemes retain the nearest-neighbor property of the ordinary FDTD, they are well suited for implementation on massively parallel computers.**

***Index Terms*—Absorbing boundary conditions, dispersive media, electromagnetic underground propagation, FDTD methods.**

I. Introduction

TRANSIENT simulation of electromagnetic wave propagation and scattering is important for a wide range of applications [1], [2]. In the microwave frequency range, the finite-difference time-domain (FDTD) [2], [3] method has become very popular. The FDTD method is ideally suited for implementation on parallel machines because only nearest-neighbor interactions are involved. Besides furnishing data directly in time domain, FDTD simulations may also be used to furnish frequency-domain data over a band of frequencies from a single run after Fourier-transforming the time-domain solution. The transient data are also particularly useful as input for a number of inverse scatering algorithms because they provide an additional dimension to the measurement data space. The data is a function not only of source-receiver position but also of frequency, which provides the redundancy required by some inverse-scattering algorithms.

In a variety of applications involving biological media, optical materials, plasma, artificial dielectrics, or earth media, the host medium is frequency dispersive. To have a realistic model for the electromagnetic wave propagation in such environments, it is prudent that we include the effect of dispersion in the media. This is especially true in simulations involving short pulses where ultrawide bandwidths are involved. A number of schemes are available to incorporate dispersion into the FDTD update [4]–[12]. Here, we will adopt the piecewise-linear recursive convolution (PLRC) approach [12]. The PLRC, besides providing a good tradeoff between computational cost and accuracy, is well suited for combining with the perfectly matched layer (PML) absorbing boundary condition to handle dispersive media modeled by multiple species Lorentz and/or Debye relaxations.

In a number of cases of technological interest, we are confronted with problems involving cylindrical geometries [13]–[21]. By far, the most common discretization scheme for the FDTD method is the central differencing scheme with staggered grids in Cartesian coordinates (Yee's scheme [2], [3]). However, when confronted with cylindrical geometries, a Cartesian grid cannot represent the geometry adequately, resulting in the well-known staircasing error. For these problems, a spatial discretization directly utilizing a cylindrical grid is the most appropriate [22]–[26]. In axisymmetric problems, the three-dimensional (3-D) cylindrical problem can be reduced to a series of 2-D problems on the ρ-z plane for each azimuthal mode field distribution, which can be solved separately with reduced computational effort [25]. In many cases however, nonaxisymmetric structures are involved, and such decomposition is not practical. Therefore, for a more flexible analysis, we employ a spatial discretization for the FDTD scheme based on a fully 3-D cylindrical grid.

In addition, absorbing boundary conditions (ABC's) need to be constructed to eliminate spurious reflections from the boundaries of the finite computational domain and to simulate the Sommerfeld radiation condition at infinity. On a cylindrical FDTD grid, the ABC's need to be constructed both for the outer radial boundary $\rho = \rho_{\max}$ and for the top and bottom boundaries $z = z_{\min}$ and $z = z_{\max}$.

In this work, we present two novel FDTD schemes in 3-D cylindrical coordinates on dispersive, inhomogeneous, and conductive (lossy) media, incorporating the PLRC approach combined with the recent extension of the PML ABC [27]–[45] to 3-D cylindrical coordinates [24], [39], [40], and further ex-

Manuscript received September 15, 1999; revised March 14, 2000. This work was supported in part by the Air Force Office of Scientific Research, Washington, DC, MURI Grant F49620-96-1-0025.

F. L. Teixeira was with the Center for Computational Electromagnetics, Department of Electrical and Computer Engineering, University of Illinois, Urbana, IL 61801-2991 USA. He is now with the Research Laboratory of Electronics, Massachusetts Institute of Technology, Cambridge, MA 02139-4307 USA (e-mail: fernando@ewt.mit.edu).

W. C. Chew is with the Center for Computational Electromagnetics, Department of Electrical and Computer Engineering, University of Illinois, Urbana, IL 61801-2991 USA (e-mail: w-chew@uiuc.edu).

Publisher Item Identifier S 0196-2892(00)05898-8.

tended to match the dispersive and conductive interior media. Most of the previously used ABC's are not suited for dispersive media because they require knowledge of the wave velocity near the grid boundary, a quantity that is not well defined in the time domain for dispersive media. In contrast to some of the previously employed ABC's, the PML is also suited for inhomogeneous media simulations as well. Moreover, being a material ABC, PML retains the nearest-neighbor interaction property of FDTD, making it very attractive for simulations on parallel machines. Recently, PML was also shown to be very effective for FDTD simulations of nonuniform cylindrical grids [24].

We extend the PML ABC to the cylindrical system using the complex coordinate stretching approach [28], [36], [38]–[43]. Two numerical schemes are developed in the time domain. The first combines the PLRC algorithm with a split-field PML approach akin to the original PML scheme of Berenger, now generalized to cylindrical coordinates [27]. The second combines PLRC with an unsplit (anisotropic medium) approach [31], whereby the cylindrical PML is introduced by means of cylindrically layered artificial constitutive tensors [39], [40]. In this scheme, the original form of Maxwell's equations is preserved. We include a comparison between the numerical stability properties of these two schemes. We then validate the PML-PLRC-FDTD schemes against pseudoanalytical solutions obtained from Sommerfeld integrals of dispersive half-space problems. To illustrate its applications, we include results from the simulation of transient scattering from buried objects in dispersive earth media and from the transient field propagation in typical geophysical environments. Because the two proposed PML-PLRC-FDTD schemes retain the nearest-neighbor property of the ordinary FDTD scheme, they are also suited for programming on parallel computers.

II. Cylindrical 3-D PML-PLRC-FDTD Split-Field Formulation

A. Modified Maxwell's Equations in Complex Space

The modified Maxwell's equations in the complex variable domain PML formulation are [28]

$$i\omega \boldsymbol{B} = \tilde{\nabla} \times \boldsymbol{E}, \tag{1}$$

$$-i\omega \boldsymbol{D} + \sigma \boldsymbol{E} = \tilde{\nabla} \times \boldsymbol{H} \tag{2}$$

for a conductive medium (static conductivity in addition to the dispersive behavior to be incorporated into the $\boldsymbol{D}$ field dependency with $\boldsymbol{E}$) and in the frequency domain ($e^{-i\omega t}$ convention). In cylindrical coordinates, we have [39], [40]

$$\tilde{\nabla} = \hat{\rho}\,\frac{\partial}{\partial \tilde{\rho}} + \hat{\phi}\,\frac{1}{\tilde{\rho}}\,\frac{\partial}{\partial \phi} + \hat{z}\,\frac{\partial}{\partial \tilde{z}}. \tag{3}$$

In the above, $\tilde{z}$ and $\tilde{\rho}$ are the spatial variables z and ρ subject to an analytic continuation (complex coordinate stretching) to a complex variable domain according to

$$\begin{aligned} \rho \to \tilde{\rho} &= \int_0^{\rho} s_\rho(\rho')\, d\rho' \\ &= \int_0^{\rho} \left(a_\rho(\rho') + i\,\frac{\Omega_\rho(\rho')}{\omega} \right) d\rho' \\ &= b_\rho(\rho) + i\,\frac{\Delta_\rho(\rho)}{\omega} \end{aligned} \tag{4}$$

$$\begin{aligned} z \to \tilde{z} &= \int_0^{z} s_z(z')\, dz' \\ &= \int_0^{z} \left(a_z(z') + i\,\frac{\Omega_z(z')}{\omega} \right) dz' \\ &= b_z(z) + i\,\frac{\Delta_z(z)}{\omega} \end{aligned} \tag{5}$$

where s_ρ and s_z are the frequency-dependent complex stretching variables, and $a_\rho(\rho)$, $\Omega_\rho(\rho)$, $a_z(z)$, and $\Omega_z(z)$ are frequency-independent variables (functions of position only). The above frequency dependence for s_ρ and s_z results in simpler time-domain equations, but other choices for the frequency-dependence (corresponding to different paths for the analytic continuation to the complex domain) of the complex stretching variables are also possible as long as they lead to absorptive effect.

The analytical continuation of Maxwell's equations to a complex domain is a general setting to understand the PML concept, allowing it to be extended to various coordinate systems [38]–[40] and to more general media such as dispersive or (bi-)anisotropic [42], [43]. This analytical continuation can be viewed as giving additional degrees of freedom s_ρ and s_z to Maxwell's equations. Its basic effect is to alter the eigenfunctions of the Maxwell's equations in such a way that originally propagating eigenfunctions are *continuously* mapped to exponentially decaying eigenfunctions. The original field and the resulting (exponentially decaying) field are homotopic to each other because (4) and (5) imply that the complex spatial coordinates $\tilde{\rho}$ and $\tilde{z}$ are continuous functions of real spatial coordinates ρ and z, respectively (regardless of whether the variables s_ρ, and s_z are continuous or not).

The decay rate inside PML is controlled by the imaginary part of s_ρ and s_z. Absorption of propagating waves is achieved by choosing Ω_z, $\Omega_\rho > 0$. In addition, faster decay of evanescent modes (if they exist) inside the PML can also be achieved by letting a_ρ, $a_z > 1$. The overall result is the reflectionless absorption of electromagnetic waves in the ρ and z directions for all frequencies and angles of incidence.

Using the relations above, the nabla operator in complex space may also be written as a modified nabla operator in the real space

$$\tilde{\nabla} = \hat{\rho}\,\frac{1}{s_\rho}\,\frac{\partial}{\partial \rho} + \hat{\phi}\,\frac{1}{\tilde{\rho}}\,\frac{\partial}{\partial \phi} + \hat{z}\,\frac{1}{s_z}\,\frac{\partial}{\partial z}. \tag{6}$$

We may also define $s_\phi = \tilde{\rho}/\rho$ and interpret it as a change on the cylindrical coordinates metric coefficients by the PML [39]. Note that this modified nabla operator above is frequency-dependent. Therefore, in the time domain, it is no longer a purely spatial operator but also a convolutional operator in time. Three distinct frequency-dependent factors are identified: s_ρ, $\tilde{\rho}$ (or s_ϕ), and s_z, each one associated with a different direction. To facilitate the solution in the time domain without convolutions, (1) and (2) may be split as follows:

$$i\omega \boldsymbol{B}_{s\rho} = \left(\hat{\rho}\,\frac{1}{s_\rho}\,\frac{\partial}{\partial \rho} \right) \times \boldsymbol{E} \tag{7}$$

$$i\omega \boldsymbol{B}_{s\phi} = \left(\hat{\phi}\,\frac{1}{\tilde{\rho}}\,\frac{\partial}{\partial \phi} \right) \times \boldsymbol{E} \tag{8}$$

$$i\omega \boldsymbol{B}_{sz} = \left(\hat{z}\,\frac{1}{s_z}\,\frac{\partial}{\partial z} \right) \times \boldsymbol{E} \tag{9}$$

$$-i\omega \boldsymbol{D}_{s\rho} + \sigma \boldsymbol{E}_{s\rho} = \left(\hat{\rho}\,\frac{1}{s_\rho}\,\frac{\partial}{\partial \rho}\right) \times \boldsymbol{H} \tag{10}$$

$$-i\omega \boldsymbol{D}_{s\phi} + \sigma \boldsymbol{E}_{s\phi} = \left(\hat{\phi}\,\frac{1}{\tilde{\rho}}\,\frac{\partial}{\partial \phi}\right) \times \boldsymbol{H} \tag{11}$$

$$-i\omega \boldsymbol{D}_{sz} + \sigma \boldsymbol{E}_{sz} = \left(\hat{z}\,\frac{1}{s_z}\,\frac{\partial}{\partial z}\right) \times \boldsymbol{H}. \tag{12}$$

By doing so, each frequency-dependent coordinate stretching factor s_ρ, $\tilde{\rho}$, s_z acquires a 1–1 relationship with a given split field. Therefore, each split field will have its time-domain evolution affected by only one corresponding stretching coordinate. In a dispersive medium

$$\boldsymbol{B} = \boldsymbol{B}_{s\rho} + \boldsymbol{B}_{s\phi} + \boldsymbol{B}_{sz} = \mu \boldsymbol{H} = \mu\left(\boldsymbol{H}_{s\rho} + \boldsymbol{H}_{s\phi} + \boldsymbol{H}_{sz}\right) \tag{13}$$

$$\boldsymbol{D} = \boldsymbol{D}_{s\rho} + \boldsymbol{D}_{s\phi} + \boldsymbol{D}_{sz} = \epsilon(\omega)\boldsymbol{E} = \epsilon(\omega)\left(\boldsymbol{E}_{s\rho} + \boldsymbol{E}_{s\phi} + \boldsymbol{E}_{sz}\right). \tag{14}$$

By using (4) and (5) and transforming back to the time domain, (7)–(12) become

$$a_\rho \frac{\partial}{\partial t}\boldsymbol{B}_{s\rho} + \Omega_\rho \boldsymbol{B}_{s\rho} = -\frac{\partial}{\partial \rho}\left(\hat{\rho} \times \boldsymbol{E}\right. \tag{15}$$

$$b_\rho \frac{\partial}{\partial t}\boldsymbol{B}_{s\phi} + \Delta_\rho \boldsymbol{B}_{s\phi} = -\hat{\phi} \times \frac{\partial}{\partial \phi}\left.\boldsymbol{E}\right) \tag{16}$$

$$a_z \frac{\partial}{\partial t}\boldsymbol{B}_{sz} + \Omega_z \boldsymbol{B}_{sz} = -\frac{\partial}{\partial z}\left(\hat{z} \times \boldsymbol{E}\right) \tag{17}$$

$$a_\rho \frac{\partial}{\partial t}\boldsymbol{D}_{s\rho} + \Omega_\rho \boldsymbol{D}_{s\rho} + a_\rho \sigma \boldsymbol{E}_{s\rho} + \Omega_\rho \sigma \int_0^t \boldsymbol{E}_{s\rho}(\tau)\,d\tau = \frac{\partial}{\partial \rho}\left(\hat{\rho} \times \boldsymbol{H}\right) \tag{18}$$

$$b_\rho \frac{\partial}{\partial t}\boldsymbol{D}_{s\phi} + \Delta_\rho \boldsymbol{D}_{s\phi} + b_\rho \sigma \boldsymbol{E}_{s\phi} + \Delta_\rho \sigma \int_0^t \boldsymbol{E}_{s\phi}(\tau)\,d\tau = \hat{\phi} \times \frac{\partial}{\partial \phi}\boldsymbol{H} \tag{19}$$

$$a_z \frac{\partial}{\partial t}\boldsymbol{D}_{sz} + \Omega_z \boldsymbol{D}_{sz} + a_z \sigma \boldsymbol{E}_{sz} + \Omega_z \sigma \int_0^t \boldsymbol{E}_{sz}(\tau)\,d\tau = \frac{\partial}{\partial z}\left(\hat{z} \times \boldsymbol{H}\right) \tag{20}$$

where we have chosen above a compact vector notation for the curl operator in cylindrical coordinates (recall that, in the cylindrical system, the angular derivative does not commute with the unit vectors $\hat{\rho}, \hat{\phi}$, since $\partial\hat{\rho}/\partial\phi = \hat{\phi}$ and $\partial\hat{\phi}/\partial\phi = -\hat{\rho}$). In terms of components, the right-hand side of (15)–(17) becomes

$$\frac{\partial}{\partial \rho}\left(\hat{\rho} \times \boldsymbol{E}\right) = -\hat{\phi}\,\frac{\partial E_z}{\partial \rho} + \hat{z}\,\frac{\partial E_\phi}{\partial \rho} \tag{21}$$

$$\hat{\phi} \times \frac{\partial}{\partial \phi}\boldsymbol{E} = \hat{z}\left(E_\phi - \frac{\partial E_\rho}{\partial \phi}\right) + \hat{\rho}\,\frac{\partial E_z}{\partial \phi} \tag{22}$$

$$\frac{\partial}{\partial z}\left(\hat{z} \times \boldsymbol{E}\right) = \hat{\phi}\,\frac{\partial E_\rho}{\partial z} - \hat{\rho}\,\frac{\partial E_\phi}{\partial z} \tag{23}$$

and similarly for (18)–(20). From (15)–(20), we see that each split-field $\boldsymbol{E}_{s\nu}$, $\boldsymbol{D}_{s\nu}$, $\boldsymbol{B}_{s\nu}$, $\boldsymbol{H}_{s\nu}$, $\nu = \rho, \phi, z$ has two components, being everywhere perpendicular to the ν direction.

The same update scheme may be used everywhere, since the interior domain (non-PML region) may be thought of as a special case of a PML with $a_\rho = a_z = 1$ and $\Omega_\rho = \Omega_z = 0$. This allows for an easier parallelization of the resulting numerical code.

B. Dispersive Models

For the dispersive model, we will assume either a Debye relaxation model or a Lorentzian relaxation model. As will be shown, the Debye model can be viewed as a special case of the Lorentzian model. The model is causa, so that the Kramers–Kronig relations are automatically satisfied. Because of this, the permittivity value will be complex, having both frequency-dependent real and imaginary parts. The imaginary part can be thought of as a frequency-dependent loss or conductivity.

An N-species Lorentzian dispersive medium is characterized by a frequency-dependent permittivity function given by

$$\epsilon(\omega) = \epsilon_0\left[\epsilon_\infty + \chi(\omega)\right] = \epsilon_0\epsilon_\infty + \epsilon_0\left(\epsilon_s - \epsilon_\infty\right)\sum_{p=1}^{N}\frac{G_p\omega_p^2}{\omega_p^2 - i2\omega\alpha_p - \omega^2} \tag{24}$$

where

- $\chi(\omega)$ medium susceptibility;
- ω_p resonant frequency for the pth species;
- α_p corresponding damping factor;
- ϵ_s, ϵ_∞ static and infinite frequency permittivities, respectively.

In the time domain, a complex susceptibility function is defined as

$$\hat{\chi}(t) = \sum_{p=1}^{P}\hat{\chi}_p(t) = \sum_{p=1}^{P} i\gamma_p e^{(-\alpha_p - i\beta_p)t}u(t) \tag{25}$$

where

$$\beta_p = \sqrt{\omega_p^2 - \alpha_p^2} \tag{26}$$

$$\gamma_p = \frac{\omega_p^2 G_p(\epsilon_s - \epsilon_\infty)}{\sqrt{\omega_p^2 - \alpha_p^2}} \tag{27}$$

and

$$\sum_{p=1}^{P} G_p = 1 \tag{28}$$

so that the time-domain susceptibility function is $\mathcal{F}^{-1}[\chi(\omega)] = \chi(t) = \Re e[\hat{\chi}(t)]$ and $\epsilon(t) = \epsilon_0[\epsilon_\infty\delta(t) + \chi(t)]$. For an N-species Debye model, the frequency-dependent permittivity function is written as

$$\epsilon(\omega) = \epsilon_0\left[\epsilon_\infty + \chi(\omega)\right] = \epsilon_0\epsilon_\infty + \epsilon_0\sum_{p=1}^{N}\frac{A_p}{1 - i\omega\tau_p}. \tag{29}$$

In this formula, A_p is the pole amplitude and τ_p is the relaxation time for the pth species. The time-domain complex susceptibility function for the Debye relaxation model can be considered as a special case of (25) when $\alpha_p > \omega_p$ and $\Im m(\beta_p) < 0$. Therefore, (25) is applicable to both models through an adequate choice of parameters. However, the Debye model requires only real arithmetic, while the Lorentz model requires complex arithmetic.

It should be pointed out that for an arbitrary linear dispersive medium, the Prony method [46] can be used to find the poles and residues of a multiterm Debye and/or Lorentz model to fit

available frequency domain data for the real and imaginary parts of the complex dielectric constant.

C. Time-Stepping Scheme

The dispersion model is included in the FDTD time-stepping scheme using the piecewise linear recursive convolution (PLRC) algorithm [12]. The intermediate steps in the derivation of the combined PML-PLRC-FDTD time-stepping scheme in cylindrical coordinates are analogous to the Cartesian case [43] and for brevity, will not be discussed here. The final equations for the PML-PLRC-FDTD time-stepping scheme for the electromagnetic fields in cylindrical coordinates are

$$\boldsymbol{H}_{s\rho}^{l+(1/2)} = -(a_\rho + \Omega_\rho \Delta_t)^{-1} \times \left[\frac{1}{\mu}\Delta_t \frac{\partial}{\partial \rho}\left(\hat{\rho} \times \boldsymbol{E}^{\boldsymbol{l}}\right) - a_\rho \boldsymbol{H}_{s\rho}^{\boldsymbol{l-}(1/2)}\right] \quad (30)$$

$$\boldsymbol{H}_{s\phi}^{l+(1/2)} = -(b_\rho + \Delta_\rho \Delta_t)^{-1} \times \left[\frac{1}{\mu}\Delta_t \left(\hat{\phi} \times \frac{\partial}{\partial \phi}\boldsymbol{E}^{\boldsymbol{l}}\right) - b_\rho \boldsymbol{H}_{s\phi}^{\boldsymbol{l-}(1/2)}\right] \quad (31)$$

$$\boldsymbol{H}_{sz}^{l+(1/2)} = -(a_z + \Omega_z \Delta_t)^{-1} \times \left[\frac{1}{\mu}\Delta_t \frac{\partial}{\partial z}\left(\hat{z} \times \boldsymbol{E}^{\boldsymbol{l}}\right) - a_z \boldsymbol{H}_{sz}^{\boldsymbol{l-}(1/2)}\right] \quad (32)$$

$$\begin{aligned}&\left[(a_\rho + \Omega_\rho \Delta_t)\lambda_0 \epsilon_0 + a_\rho \sigma \Delta_t\right] \boldsymbol{E}_{s\rho}^{\boldsymbol{l+1}} \\ &\quad = \Delta_t \frac{\partial}{\partial \rho}\left(\hat{\rho} \times \boldsymbol{H}^{l+(1/2)}\right) + a_\rho \boldsymbol{D}_{s\rho}^{\boldsymbol{l}} - \sigma \Omega_\rho \Delta_t \boldsymbol{F}_{s\rho}^{\boldsymbol{l}} \\ &\qquad - (a_\rho + \Omega_\rho \Delta_t)\epsilon_0\left(\lambda_1 \boldsymbol{E}_{s\rho}^{\boldsymbol{l}} + \boldsymbol{P}_{s\rho}^{\boldsymbol{l}}\right) \end{aligned} \quad (33)$$

$$\begin{aligned}&\left[(b_\rho + \Delta_\rho \Delta_t)\lambda_0 \epsilon_0 + b_\rho \sigma \Delta_t\right] \boldsymbol{E}_{s\phi}^{\boldsymbol{l+1}} \\ &\quad = \Delta_t \left(\hat{\phi} \times \frac{\partial}{\partial \phi}\boldsymbol{H}^{l+(1/2)}\right) + b_\rho \boldsymbol{D}_{s\rho}^{\boldsymbol{l}} - \sigma \Delta_\rho \Delta_t \boldsymbol{F}_{s\phi}^{\boldsymbol{l}} \\ &\qquad - (b_\rho + \Delta_\rho \Delta_t)\epsilon_0\left(\lambda_1 \boldsymbol{E}_{s\phi}^{\boldsymbol{l}} + \boldsymbol{P}_{s\phi}^{\boldsymbol{l}}\right) \end{aligned} \quad (34)$$

$$\begin{aligned}&\left[(a_z + \Omega_z \Delta_t)\lambda_0 \epsilon_0 + a_z \sigma \Delta_t\right] \boldsymbol{E}_{sz}^{\boldsymbol{l+1}} \\ &\quad = \Delta_t \frac{\partial}{\partial z}\left(\hat{z} \times \boldsymbol{H}^{l+(1/2)}\right) + a_z \boldsymbol{D}_{sz}^{\boldsymbol{l}} - \sigma \Omega_z \Delta_t \boldsymbol{F}_{sz}^{\boldsymbol{l}} \\ &\qquad - (a_z + \Omega_z \Delta_t)\epsilon_0\left(\lambda_1 \boldsymbol{E}_{sz}^{\boldsymbol{l}} + \boldsymbol{P}_{sz}^{\boldsymbol{l}}\right). \end{aligned} \quad (35)$$

On the right-hand side of (33)–(35), the other pertinent quantities are updated as follows:

$$\boldsymbol{D}_{s\nu}^{\boldsymbol{l}} = \epsilon_0\left(\lambda_0 \boldsymbol{E}_{s\nu}^{\boldsymbol{l}} + \lambda_1 \boldsymbol{E}_{s\nu}^{\boldsymbol{l-1}} + \boldsymbol{P}_{s\nu}^{\boldsymbol{l-1}}\right) \quad (36)$$

$$\boldsymbol{F}_{s\nu}^{\boldsymbol{l}} = \boldsymbol{F}_{s\nu}^{\boldsymbol{l-1}} + \tfrac{1}{2}\left(\boldsymbol{E}_{s\nu}^{\boldsymbol{l}} + \boldsymbol{E}_{s\nu}^{\boldsymbol{l-1}}\right)\Delta_t \quad (37)$$

$$\boldsymbol{Q}_{p,\,s\nu}^{\boldsymbol{l}} = \left(\hat{\zeta}_p^a - \hat{\zeta}_p^b\right)\boldsymbol{E}_{s\nu}^{\boldsymbol{l}} + \hat{\zeta}_p^b \boldsymbol{E}_{s\nu}^{\boldsymbol{l-1}} + \boldsymbol{Q}_{p,\,s\nu}^{\boldsymbol{l-1}} e^{-i\tilde{\omega}_p \Delta_t} \quad (38)$$

$$\boldsymbol{P}_{s\nu}^{\boldsymbol{l}} = \sum_{p=1}^{P} \Re e\left[\boldsymbol{Q}_{p,\,s\nu}^{\boldsymbol{l}} e^{-i\tilde{\omega}_p \Delta_t}\right] \quad (39)$$

where ν is replaced with ρ, ϕ, or z. Hence, (30)–(39) constitute the complete updating scheme for the electromagnetic fields in the split-field PML-PLRC-FDTD formulation. The complex parameters $\hat{\zeta}_p^a$, $\hat{\zeta}_p^b$ are the zeroth- and first-order moments of the (time-domain) complex susceptibility functions taken over a time-discretization interval, λ_0 and λ_1 are real constants that give instantaneous corrections for the dispersive dielectric constant, and $\tilde{\omega}_p$ are the complex frequency poles of the model. These constants depend on the particular choice of parameters for the Debye or Lorentz dispersive model chosen. For the pth species, they are explicitly given in terms of the α_p, β_p, γ_p parameters as follows:

$$\hat{\zeta}_p^a = \int_0^{\Delta_t} \hat{\chi}_p(t)\,dt = \frac{i\gamma_p}{\alpha_p + i\beta_p}\left[1 - e^{-(\alpha_p + i\beta_p)\Delta_t}\right] \quad (40)$$

$$\begin{aligned}\hat{\zeta}_p^b &= \int_0^{\Delta_t} t\hat{\chi}_p(t)\,dt \\ &= \frac{i\gamma_p}{\Delta_t\,(\alpha_p + i\beta_p)^2} \\ &\quad \times \left\{1 - \left[(\alpha_p + i\beta_p)\,\Delta_t + 1\right]e^{-(\alpha_p + i\beta_p)\Delta_t}\right\} \end{aligned} \quad (41)$$

$$\lambda_0 = \epsilon_\infty + \sum_{p=1}^{P} \Re e\left[\hat{\zeta}_p^a - \hat{\zeta}_p^b\right] \quad (42)$$

$$\lambda_1 = \sum_{p=1}^{P} \Re e\left[\hat{\zeta}_p^b\right] \quad (43)$$

$$\tilde{\omega}_p = \beta_p - i\alpha_p. \quad (44)$$

III. Cylindrical Grid 3-D PML-PLRC-FDTD in Dispersive Media: Unsplit Field (Anisotropic Medium) Formulation

The unsplit field formulation of PML is an alternative formulation of PML, where the spatial operators in the Maxwell's equations retain their usual form, and the constitutive relations are modified instead. The resultant electromagnetic fields inside the PML can be associated with those of an anisotropic medium with artificial electric and magnetic constitutive tensors. The existence of such a dual, anisotropic medium PML formulation stems from the metric invariance of Maxwell's equations, as discussed in [47], [48].

In the case of 3-D cylindrical coordinates, the PML constitutive tensors matched to a homogeneous nondispersive medium characterized by constitutive parameters ϵ, μ, are written as [39]

$$\bar{\boldsymbol{\epsilon}}_{\mathrm{PML}} = \epsilon \overline{\boldsymbol{\Lambda}}_{[\rho,\,\phi,\,z]}(\rho,\,z;\,\omega) \quad (45)$$

$$\bar{\boldsymbol{\mu}}_{\mathrm{PML}} = \mu \overline{\boldsymbol{\Lambda}}_{[\rho,\,\phi,\,z]}(\rho,\,z;\,\omega) \quad (46)$$

with

$$\overline{\boldsymbol{\Lambda}}_{[\rho,\,\phi,\,z]}(\rho,\,z;\,\omega) = \boldsymbol{\phi}_\phi \boldsymbol{\phi}_\phi \frac{\rho s_z s_\rho}{\tilde{\rho}} + \boldsymbol{z}_z \boldsymbol{z}_z \frac{\tilde{\rho} s_\rho}{\rho s_z} + \boldsymbol{\rho}_\rho \boldsymbol{\rho}_\rho \frac{\tilde{\rho} s_z}{\rho s_\rho} \quad (47)$$

and $\tilde{\rho}$, s_ρ, s_z, as defined earlier.

Since the perfect matching condition for the PML anisotropic medium is a *local* condition in space (i.e., a boundary condition), and it is valid for all frequencies, the PML can be extended to match either or both an inhomogeneous or a dispersive interior medium with constitutive parameters μ and $\epsilon(\boldsymbol{r}, \omega)$ in a transparent manner with $\bar{\boldsymbol{\epsilon}}_{\mathrm{PML}}$ given as

$$\bar{\boldsymbol{\epsilon}}_{\mathrm{PML}} = \epsilon(\boldsymbol{r}, \omega)\overline{\boldsymbol{\Lambda}}_{[\rho,\,\phi,\,z]}(\rho,\,z;\,\omega) \quad (48)$$

and $\bar{\boldsymbol{\mu}}_{\mathrm{PML}}$ given as before in (46). Such constitutive parameters produce a PML medium matched to the interior medium for all frequencies and angles of incidence [39].

In the unsplit field formulation, we write for Maxwell's equations

$$i\omega\mu \overline{\boldsymbol{\Lambda}}_{[\rho,\,\phi,\,z]} \cdot \boldsymbol{H} = \nabla \times \boldsymbol{E} \quad (49)$$

$$-i\omega\left(1+\frac{i\sigma}{\omega\epsilon(\omega)}\right)\epsilon(\omega)\overline{\boldsymbol{\Lambda}}_{[\rho,\phi,z]}\cdot\boldsymbol{E}=\nabla\times\boldsymbol{H} \quad (50)$$

which may be written, in terms of auxiliary fields $\boldsymbol{B}_a$, $\boldsymbol{D}_a$, and $\boldsymbol{E}_a$, as

$$i\omega\mu\boldsymbol{H}_a=\nabla\times\boldsymbol{E} \quad (51)$$

$$-i\omega\boldsymbol{D}_a+\sigma\boldsymbol{E}_a=\nabla\times\boldsymbol{H} \quad (52)$$

where, by definition, $\boldsymbol{H}_a=\overline{\boldsymbol{\Lambda}}_{[\rho,\phi,z]}\cdot\boldsymbol{H}$, $\boldsymbol{D}_a=\overline{\boldsymbol{\Lambda}}_{[\rho,\phi,z]}\cdot\boldsymbol{D}$, and $\boldsymbol{E}_a=\overline{\boldsymbol{\Lambda}}_{[\rho,\phi,z]}\cdot\boldsymbol{E}$. The auxiliary fields are introduced as a computational convenience. This is because, by comparing (51)–(52) with (1)–(2), it is evident that the update for the auxiliary fields $\boldsymbol{B}_a$, $\boldsymbol{D}_a$, $\boldsymbol{E}_a$ is just an unsplit version of the previous update equations given by (30)–(39), and with $s_\rho=s_z=1$, i.e.,

$$\boldsymbol{H}_a^{l+(1/2)}=\boldsymbol{H}_a^{l-(1/2)}-\tfrac{1}{\mu}\,\Delta_t\nabla\times\boldsymbol{E}^l \quad (53)$$

$$(\lambda_0\epsilon_0+\sigma\Delta_t)\,\boldsymbol{E}_a^{l+1}=\Delta_t\nabla\times\boldsymbol{H}^{l+(1/2)}+\boldsymbol{D}_a^l-\epsilon_0\left(\lambda_1\boldsymbol{E}_a^l+\boldsymbol{P}_a^l\right) \quad (54)$$

and with the other pertinent auxiliary quantities on the right hand side of (54) being updated analogously as in (36), (38), and (39)

$$\boldsymbol{D}_a^l=\epsilon_0\left[\lambda_0\boldsymbol{E}_a^l+\lambda_1\boldsymbol{E}_a^{l-1}+\boldsymbol{P}_a^{l-1}\right] \quad (55)$$

$$\boldsymbol{Q}_{a,p}^l=\left(\hat{\zeta}_p^a-\hat{\zeta}_p^b\right)\boldsymbol{E}_a^l+\hat{\zeta}_p^b\boldsymbol{E}_a^{l-1}+\boldsymbol{Q}_{a,p}^{l-1}e^{-i\tilde{\omega}_p\Delta_t} \quad (56)$$

$$\boldsymbol{P}_a^l=\sum_{p=1}^{P}\Re e\left[\boldsymbol{Q}_{a,p}^l e^{-i\tilde{\omega}_p\Delta_t}\right]. \quad (57)$$

Again, p is the number of the species on the dispersive model used, and the constants $\hat{\zeta}_p^a$, $\hat{\zeta}_p^b$, λ_0 and λ_1, and $\tilde{\omega}_p$ are defined as before and depend on the particular choice of parameters adopted for the Debye or Lorentz dispersive model.

The update scheme is incomplete without specifying how one updates the original fields from the auxiliary ones. This is done using the definitions of the auxiliary fields themselves, i.e.,

$$\boldsymbol{E}=\overline{\boldsymbol{\Lambda}}_{[\rho,\phi,z]}^{-1}\cdot\boldsymbol{E}_a \quad (58)$$

$$\boldsymbol{H}=\overline{\boldsymbol{\Lambda}}_{[\rho,\phi,z]}^{-1}\cdot\boldsymbol{H}_a \quad (59)$$

$$\boldsymbol{D}=\overline{\boldsymbol{\Lambda}}_{[\rho,\phi,z]}^{-1}\cdot\boldsymbol{D}_a \quad (60)$$

or, in terms of components

$$E_\rho=\frac{s_\rho}{s_\phi s_z}E_{a,\rho} \quad (61)$$

$$H_\rho=\frac{s_\rho}{s_\phi s_z}H_{a,\rho} \quad (62)$$

$$D_\rho=\frac{s_\rho}{s_\phi s_z}D_{a,\rho} \quad (63)$$

and analogously for the other components by cyclic permutation of indices.

A simple system of first-order differential equations can be derived from the above equations through the use of other sets of auxiliary fields $\boldsymbol{E}_e$, $\boldsymbol{H}_e$, $\boldsymbol{D}_e$, so that (61) is replaced by

$$(i\omega s_z)\,E_{e,\rho}=(i\omega s_\rho)\,E_{a,\rho} \quad (64)$$

$$(i\omega s_\phi)\,E_\rho=i\omega E_{e,\rho} \quad (65)$$

and analogously for (62) and (63). In the time domain, the previous equations become

$$\left(a_z\frac{\partial}{\partial t}+\Omega_z\right)E_{e,\rho}=\left(a_\rho\frac{\partial}{\partial t}+\Omega_\rho\right)E_{a,\rho} \quad (66)$$

$$\left(b_\rho\frac{\partial}{\partial t}+\Delta_\rho\right)E_\rho=\frac{\partial}{\partial t}E_{e,\rho}. \quad (67)$$

The time update equations for the original field in terms of the auxiliary field then become

$$(a_z+\Omega_z\Delta_t)\,E_{e,\rho}^l=a_zE_{e,\rho}^{l-1}+(a_\rho+\Omega_\rho\Delta_t)\,E_{a,\rho}^l-a_\rho E_{e,\rho}^{l-1} \quad (68)$$

$$(b_\rho+\Delta_\rho\Delta_t)\,E_\rho^l=b_\rho E_\rho^{l-1}+E_{e,\rho}^l-E_{e,\rho}^{l-1} \quad (69)$$

where, for simplicity, we have used a backward Euler scheme. A central differencing scheme is also possible. In this case, a linear interpolation can be used for the constant terms to maintain second-order accuracy in time. Analogous update equations apply for the other field components. In the case of the $\boldsymbol{H}$ field components, however, one may incorporate one of the complex stretching variables of (62) already into a modified (lossy) update for (51) instead. In this case, one less auxiliary field is necessary. Together with (53)–(57), these equations constitute the complete update scheme for the electromagnetic fields in the unsplit PML-PLRC-FDTD formulation.

IV. Issues on the Spatial Discretization

The adopted spatial discretization on the cylindrical grid uses a central differencing scheme with staggered grids. Fig. 1 depicts the location of the electromagnetic field components associated with a given point $P=(i,\,j,\,k)$ on the cylindrical grid. This grid is orthogonal everywhere and retains a clear association with the usual Yee FDTD scheme in Cartesian coordinates since the electric field components are located at the edges of the primary grid, and the magnetic field components are located at the faces of the primary grid, or equivalently, at the edges of the dual grid staggered from the primary one. Because each component is located at a different position of space, as illustrated in Fig. 1(a), the discretized space presents an inherent fuzziness that becomes clear for inhomogeneous media when it is necessary to define its constitutive parameters ϵ and μ as a function of position. In most practical instances, this is usually mitigated by the fact that the discretization size is chosen small in terms of the minimum characteristic wavelength or in terms of the minimum geometric features (inhomogeneities).

Around the axial singularity at $r=0$, we adopt triangular (degenerate) cells adjacent to the axis, associated with the update for the H_z component nearest to $r=0$. Due to the staggered nature of the grid, only one of the fields H_z or E_z coincides with the z axis. In our scheme, we choose the E_z component to be located right on $r=0$ and update it through the use of Ampere's law on a small circular contour around the axis. Also located at $r=0$ are E_ϕ and H_ρ, which, by symmetry, can be shown to be zero. Moreover, these fields are not used to update the remaining components (this follows from the triangular geometry of the degenerated cells nearest to the axis and also from the symmetry of the problem which enforces $\partial/\partial\phi=0$ at $r=0$). The location of the field components near the z axis is illustrated in Fig. 1(b). The update of the remaining components H_ϕ and E_ρ, nearest to (which are not right at) the z axis does not need to be modified from the normal update. When updating H_z and H_ϕ nearest the singularity, special care is taken to explicitly enforce the overall reciprocity between the $\boldsymbol{E}$ and $\boldsymbol{H}$ updates by constructing discrete curl operator matrices for the primary and

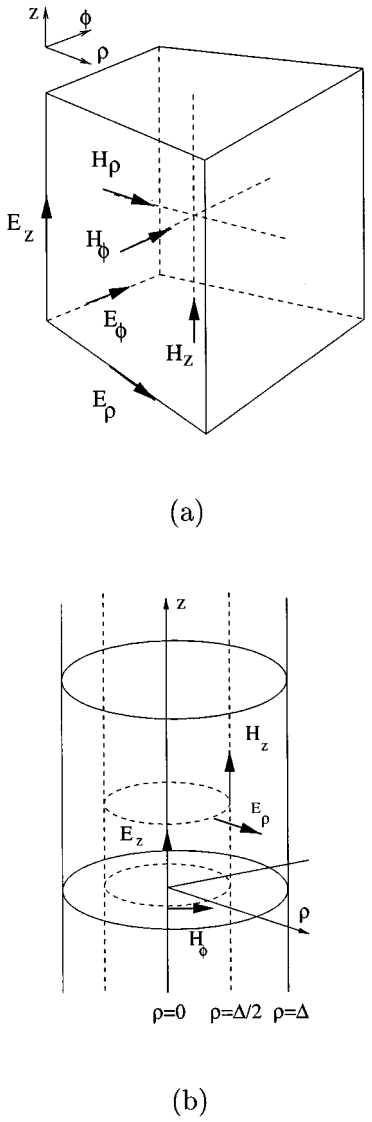

Fig. 1. (a) Interior unit cell of the staggered grid scheme for spatial discretization of electromagnetic fields on the cylindrical grid. (b) Degenerate cells adjacent to the z axis of the staggered grid scheme for spatial discretization of electromagnetic fields on the cylidrical grid. Only the nonzero components are shown.

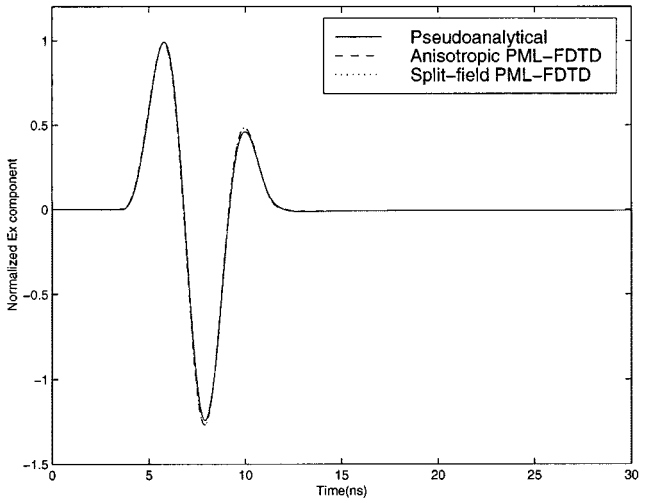

Fig. 2. Comparison of the split-field and anisotropic PML results against a pseudo-analytical solution using Sommerfeld integration. The receiver is buried inside a dispersive medium (Puerto Rico clay loam with 5% moisture).

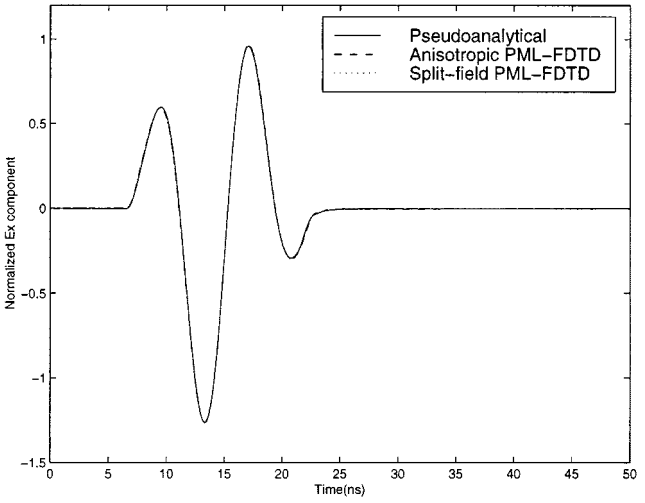

Fig. 3. Comparison of the split-field and anisotropic PML results against a pseudo-analytical solution using Sommerfeld integration. The receiver is buried inside a dispersive medium (Puerto Rico clay loam with 2.5% moisture).

dual grids that are transpose to each other [48]. This last condition is important to preserve key theorems of the continuum theory and ensure stability of the scheme [48]–[51].

V. Numerical Results

FDTD codes have been written using both formulations described in the previous sections. In the case of the split-field formulation, the fields are split everywhere so that the code can be easily parallelized.

A. Validation

To first validate the formulation, the results from the FDTD simulation for a homogeneous dispersive half-space problem with conductive loss are compared against a pseudo-analytical solution. The pseudo-analytical solution is obtained by first numerically integrating the frequency-domain Sommerfeld integrals of the half-space problem for many excitation frequencies [2]. The result is then multiplied by the spectrum of the source pulse, and subsequently inverse-Fourier transformed to yield the time-domain solution. Fig. 2 compares the results for the FDTD simulations in a dispersive half-space against this pseudo-analytical solution. The half space dispersion parameters are obtained by fitting a two-species ($P = 2$) Debye model to the experimental data reported by Hipp [52] for the Puerto Rico type of clay loams (with 5% moisture content), which can be found in [43]. The domain is discretized using a $(N_\rho, N_\phi, N_z) = (40, 80, 60)$ grid. The PML is set up using 14 cells both in ρ and z directions and a quadratic taper for the Ω_ρ and Ω_z variables. The cell discretization size is uniform in the ρ and z directions $\Delta\rho = \Delta z = 3.75$ cm. The half space occupies 50% of the vertical height of the simulation region. The source is a z-oriented electric Hertzian dipole located at the grid point $(0.1N_\rho, 0.1N_\phi, 0.6N_z)$, while the receiver is located

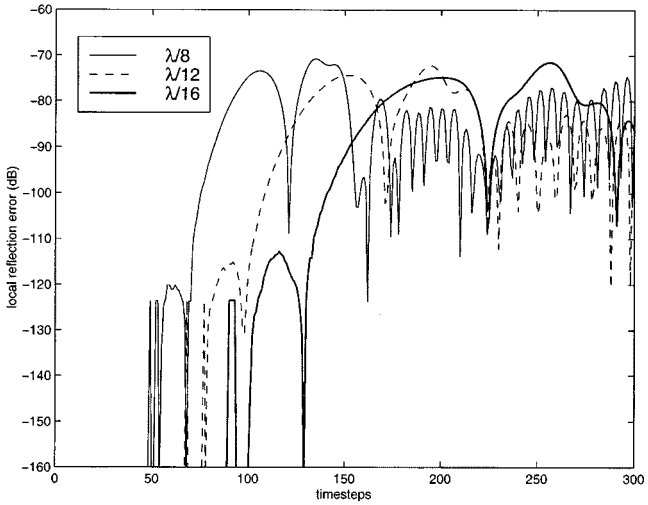

Fig. 4. Local reflection error within test grid observed over the first 300 time steps for an eight-layer cylindrical PML. Three different angular resolutions are considered. See text for details.

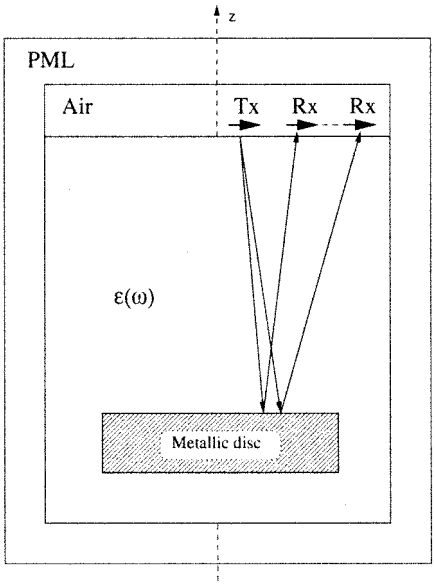

Fig. 5. Schematics of the geometry for the simulation of the electromagnetic response of a circular metallic disc buried on a dispersive soil with conductive loss. The dimensions are indicated in the text.

at $(0.3N_\rho, 0.6N_\phi, 0.4N_z)$. The excitation pulse is the first derivative of a modified Blackman–Harris pulse [34], centered at 200 MHz. The receiver is deliberately buried in the half space so that it is more sensitive to the dispersive properties of the medium. This figure shows a very good agreement between the formulations. Note that the source-receiver positioning is such that the pulse passes through the $\rho = 0$ axis. This verifies the accuracy and stability of the axis singularity treatment in our discretization scheme.

Fig. 3 depicts the results of a simulation on a similar soil, but with a lower moisture content (2.5%). The simulation grid has the same size as before, but the PML buffer region is reduced to 12 cells in both z and ρ directions. Furthermore, the center frequency is reduced to 100 MHz, while

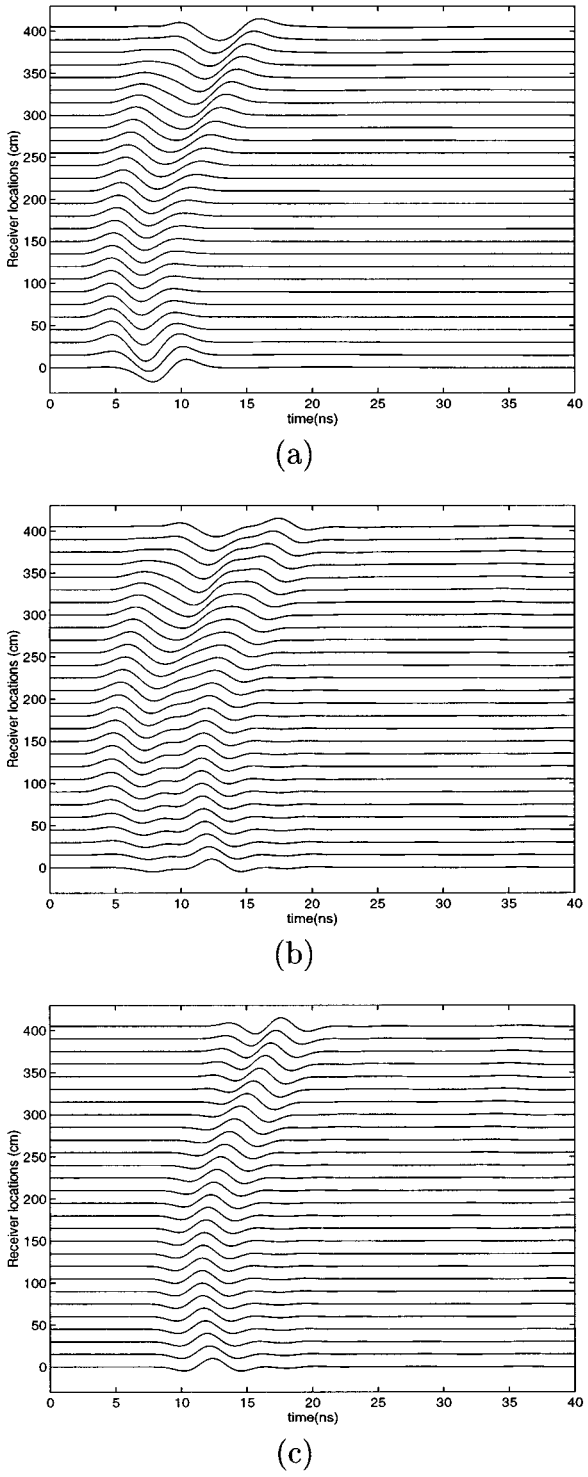

Fig. 6. Waveforms for a horizontal electric dipole on top of a Debye medium with a metallic disc buried in it. (a) Incident field, (b) total field, and (c) scattered field. The ordinate indicates the receiver location with respect to the initial position.

keeping the same discretization size $\Delta\rho = \Delta z = 3.75$ cm (implying a higher grid resolution in terms of wavelength). The source-receiver separation is now increased, with the source (again a z-oriented, electric Hertzian dipole) being located at the grid point $0.2N_\rho, 0.1N_\phi, 0.7N_z)$, and the receiver at $((0.6N_\rho, 0.6N_\phi, 0.3N_z)$. The half-space occupies 50% of the

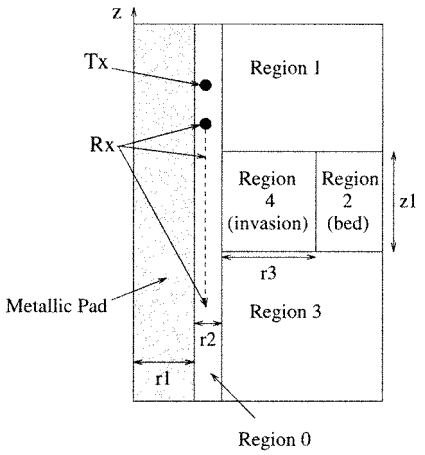

Fig. 7. Cross-sectional view of a cylindrical fluid column, backed by a metallic pad, penetrating a three-layer environment with an invaded middle layer (thin bed zone). The dimensions and media parameters are indicated in the text.

vertical height of the simulation region. Again, a very good agreement between the formulations is obtained.

B. Cylindrical PML Reflection Analysis

In the continuum, the PML is reflectionless. In practical applications, however, because there is a need to work with a PML of finite thickness and because of the discretization process, the PML is not reflectionless anymore. A small spurious reflection is present. This is discussed in more detail in [53]. To accurately quantify the amount of spurious reflection caused by the discrete cylindrical PML, we follow a methodology discussed in [3], [54]. Two cylindrical FDTD grids are used: a test domain Ω_T and a benchmark domain Ω_B. To isolate the effects of the spurious reflection from the cylindrical PML, a 2-D grid is considered here (reflections from the z direction corresponds to spurious reflections from a planar PML interface, already extensively studied before). The test domain includes the cylindrical PML, and the benchmark domain has untreated boundaries but a much larger size. The outer boundaries of Ω_B are defined so that its spurious reflections can be windowed out and causally isolated during the time-stepping when comparing simulations on the two grids. Therefore, the grid Ω_B effectively simulates an infinite grid. Discrepancies between the computed field values in the two grids are produced by spurious reflection from the PML in the Ω_T domain.

Fig. 4 presents the local reflection errors obtained from an eight-layer cylindrical PML. Three results are presented, corresponding to three different angular grid resolutions. The simulations employ a (hard) line source excited by a Blackmann–Harris pulse with central frequency $f_c = 300$ MHz. The local reflection error is obtained by field sampling at two grid cells away from the free-space/PML interface of the Ω_T domain. The line source location is eight cells away from the free-space/PML interface. The radial resolution in all cases is fixed at $\Delta\rho = \lambda_c/16$. The free-space/PML interface in Ω_T is situated at $\rho_0 = 4\lambda_c$. The eight-layer PML employs a fourth-order tapered profile on the imaginary part of the stretching variables and no stretching on the real part. The benchmark domain is truncated at $\rho = 8\lambda_c$.

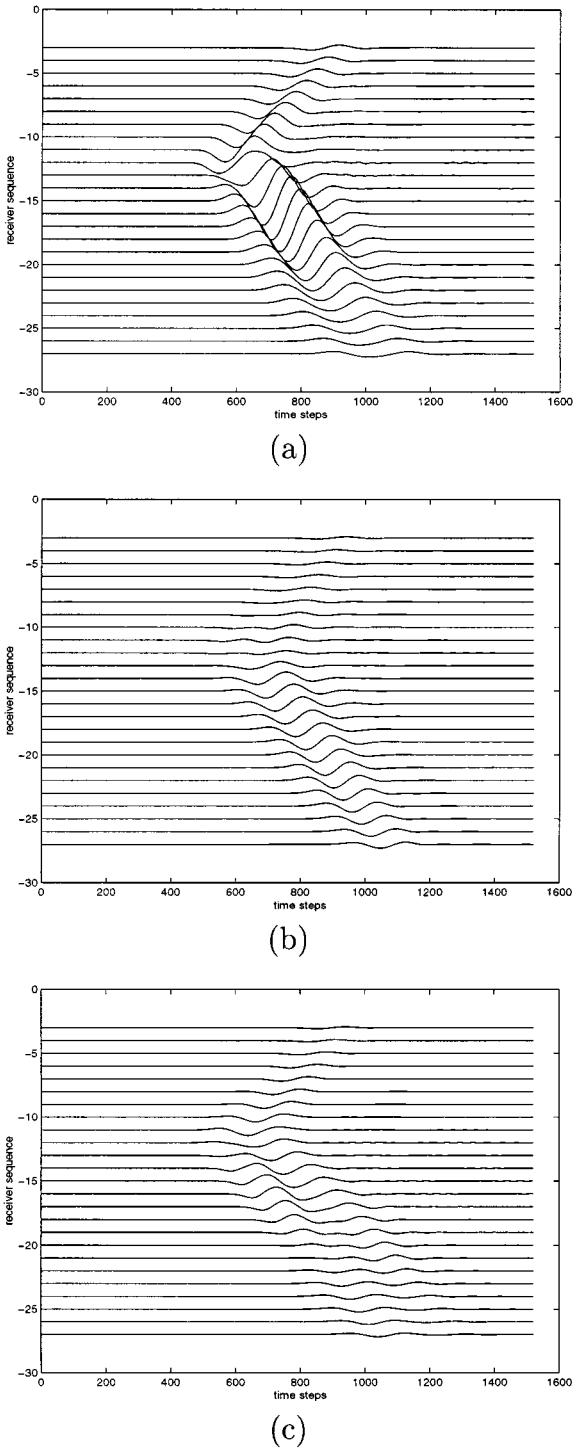

Fig. 8. Voltage traces (difference signal) for the geometry in Fig. 7 with (a) noninvaded bed zone, (b) homogeneous invasion, and (c) inhomogeneous invasion. Traces are sequentially offset according to receiver location. The transmitter is kept fixed.

The local error data is normalized to the peak value of the incident pulse at the sampling location. The three angular resolutions considered correspond to values of $\Delta\phi$ such that $\rho_0\Delta\phi = \lambda/8, \lambda/12, \lambda/16$, where ρ_0 is at the free-space/PML interface in Ω_T. The results of Fig. 4 exemplify the very low reflection levels incurred by the cylindrical PML. A reflection

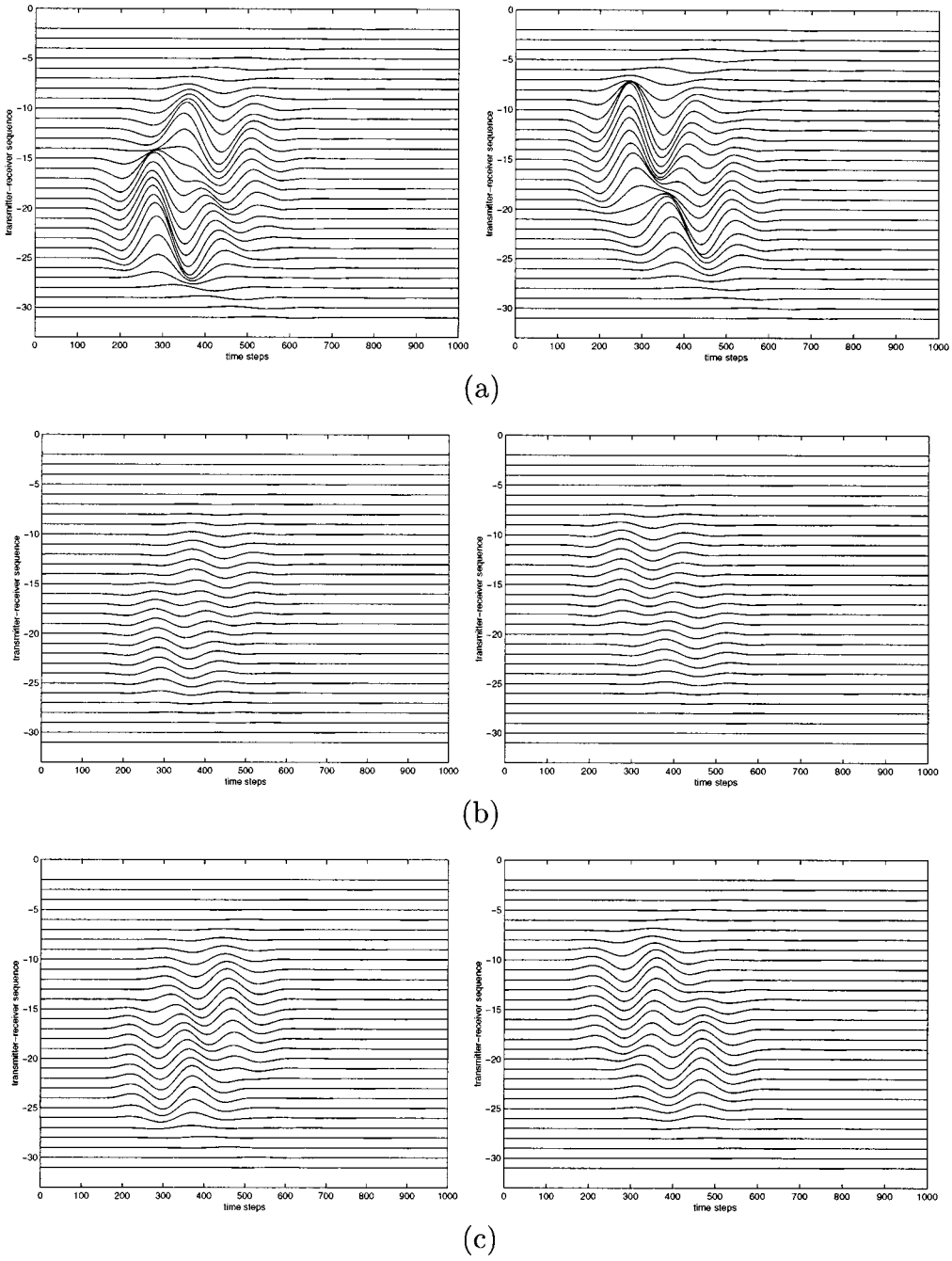

Fig. 9. Voltage traces (difference signal) for the geometry in Fig. 7 with (a) noninvaded bed zone, (b) homogeneous invasion, and (c) inhomogeneous invasion. A pair of transmitters and a pair of receivers move together downwards along the formation, modeling an antenna array in a logging tool. Traces are sequentially offset according to the antenna array location. Traces at the left correspond to the signal at the top receiver, and traces at the right to the signal at the bottom receiver.

level better than -70 dB is obtained with the 8-layer cylindrical PML.

C. Buried Object in Dispersive Soil

Next, we simulate the electromagnetic response of a cylindrical disc buried in a 2.5% moisture soil modeled with a two-species Debye model. The grid size is $(N_\rho, N_\phi, N_z) = (100, 160, 45)$. The source is a horizontal (ρ-directed) dipole located at the grid point $(i_\rho, i_\phi, i_z) = (30, 80, 30)$, just above the air-ground interface, located at $i_z = 29$. The E_x field is sampled through a radial measurement line (approximately 2 m long) running from the initial point ($(i_\rho, i_\phi, i_z) = (10, 96, 30)$ to the end point (i_ρ, i_ϕ, i_z) =(66, 96, 30). This simulates a common-source radargram configuration usual in ground-penetrating radar (GPR) applications [55]–[64]. The geometry of this problem is illustrated in Fig. 5. The spatial discretization size is uniform in the z and ρ directions, $\Delta\rho = \Delta z = 3.75$ cm. The time step used is 3.923 ps. The cylindrical disc is made up of a good conductor ($\sigma = 10^6$) and is buried such that its top is 52.5 cm below the air-ground interface. It has a 1.12 m radius and a 7.5 cm height and is centered at the z axis. The unsplit field PML consists of ten cells with a quadratic profile both at

the outer radial boundary (for the Ω_ρ variable) and at the top and bottom terminations (for the Ω_z variable). The source pulse is again the first derivative of a slightly modified Blackman-Harris pulse, having a finite support and centered at 200 MHz. Fig. 6 depicts the resulting waveforms as a function of position. Each waveform is normalized to its maximum value. Presented are the waveforms for the incident field (no object buried in the soil), the total field, and the scattered field from the buried conducting cylinder.

D. Borehole Example 1

In Fig. 7, we depict the geometry of a three-layer host medium penetrated by a circular column (metallic pad surrounded by a standoff region).

Three cases are simulated: 1) a case where the mid layer (bed zone, Region 2) contains a homogeneous invaded zone (Region 4); 2) a case where the invaded zone is inhomogeneous, with the permittivity in Region 4 varying linearly from those in Region 0 and Region 2; and c) a case with no invaded zone, i.e., Region 4 having the same constitutive parameters as Region 2. The computational grid has $(N_\rho, N_\phi, N_z) = (35, 80, 150)$ including 10-layer PML's at its top and bottom regions and along the outer radial direction. The grid discretization size is $\Delta_\rho = \Delta_z = 0.3$ cm. The source excites a derivative of the Blackmann–Harris pulse centered at 1 GHz, typical frequency of the Electromagnetic Propagation Tool (EPT[1]). Such geophysical sensing tools are designed to measure high dielectric constants for delineating fresh water bearing zones from hydrocarbon bearing zones [65], [66]. The constitutive parameters for the different regions are given by $(\epsilon_0, \sigma_0) = (25, 0.5)$, $(\epsilon_1, \sigma_1) = (\epsilon_3, \sigma_3) = (15, 0.3)$, $(\epsilon_2, \sigma_2) = (5, 0.1)$. Region 4 is the invasion, which in the case of a homogeneous invasion is considered to have $(\epsilon_4, \sigma_4) = (12, 0.3)$. In the case of an inhomogeneous invasion, we set $\sigma_4 = 0.3$ and set ϵ_4 to vary linearly between the values of ϵ_0 and ϵ_2. The media are considered nonmagnetic so that $\mu = \mu_0$ everywhere. The borehole has a diameter $d_1 = 14.4$ cm, and the standoff region is 1.2 cm thick. When present, the invaded zone penetrates $d_2 = 6$ cm deep into the bed zone, which is $z_1 = 12$ cm thick. Both source and receiver are polarized along the azimuthal direction. The dipole transmitter is fixed at 16.5 cm above the bed boundary, and the dipole receiver moves vertically in the borehole in a common source configuration with the transmitter at the top position. Fig. 8 shows the difference traces of the reflected signals from the three cases considered. The reference signal corresponds to a homogeneous host media with (ϵ_1, σ_1). The reflected signal caused by the bed discontinuty is clearly visible in those figures. We also observe that the invasion significantly reduces the signal reflected from the bed discontinuity (the same normalization factor is used in all plots). In addition, a gradual (inhomogeneous) invasion zone [case (b)] has the effect of smoothing out the reflected signal.

Fig. 9 shows the difference traces for the same geometry but now with a different transmitter-receiver configuration, consisting of two transmitters and two receivers (magnetic dipoles polarized along the azimuthal direction). The receivers are placed 3 cm vertically apart. The top transmitter is located at 4.5 cm above the top receiver, and the bottom transmitter is located at 4.5 cm below the bottom receiver (symmetric configuration). This configuration models an antenna array used in practical logging tools. The small transmitter-receiver spacings and the configuration of the tool is because the electromagnetic energy usually has a low penetration depth in usual geophysical environments at 1 GHz. The traces depicted in Fig. 9 are taken sequentially as the transmitters and receiver move downward inside the formation. The left traces correspond to the difference voltage at the top receiver, and the right trace to the difference trace at the bottom receiver. The first (top) trace corresponds to the center of the tool being at 10.5 cm above the bed boundary and the last (bottom) trace shown corresponds to the center of the tool being at 1.5 cm below the bottom bed boundary. Further traces at lower positions are redundant due to the vertical symmetry of the transmitter-receiver configuration and the geophysical formation considered. The three sets of voltage traces depicted correspond, again, to a case of a noninvaded bed zone, a case with homogeneous invasion, and a case with a inhomogeneous invasion, respectively.

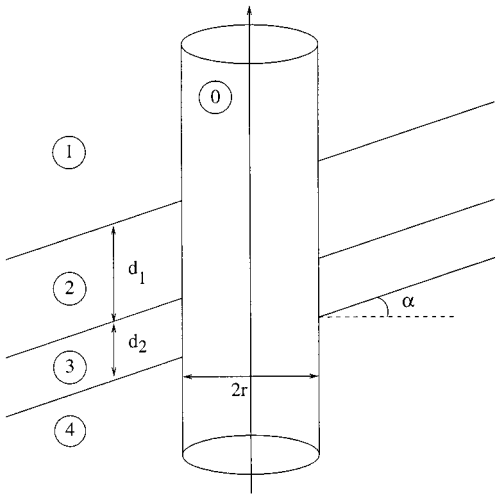

Fig. 10. Circular column penetrating a host medium with dipping layers. The media parameters are indicated in the text.

E. Borehole Example 2: Dipping Beds

In the next example, we consider a circular column penetrating a host medium with dipping layers, as indicated in Fig. 10. The dip is characterized by the angle α, chosen as $\alpha = 45^0$. The parameters (ϵ_r, σ) for the media indicated in Fig. 9 are: medium 0: (20, 0.01), medium 1: (2, 0.01), medium 2: (20, 1), medium 3: (5, 0.05), and medium 4: (2, 0.01). The radius of the cylindrical column is $r = 0.12$ m, and the vertical dimensions d_1 and d_2 indicated in the Fig. 10 are 0.28 m and 0.14 m, respectively. The source is a vertical Hertzian electric dipole located slightly off-axis (two grid points from $\rho = 0$), which launches a pulse centered at $f_c = 500$ kHz. At such a low frequency, the skin depths δ_i of the media considered are much smaller that the corresponding wavelengths λ_i. As a result, the smallest skin depth (medium 3 with $\delta_3 = 0.71$ m) dictates the required resolution for the spatial discretization

[1]Trademark of Schlumberger Ltd.

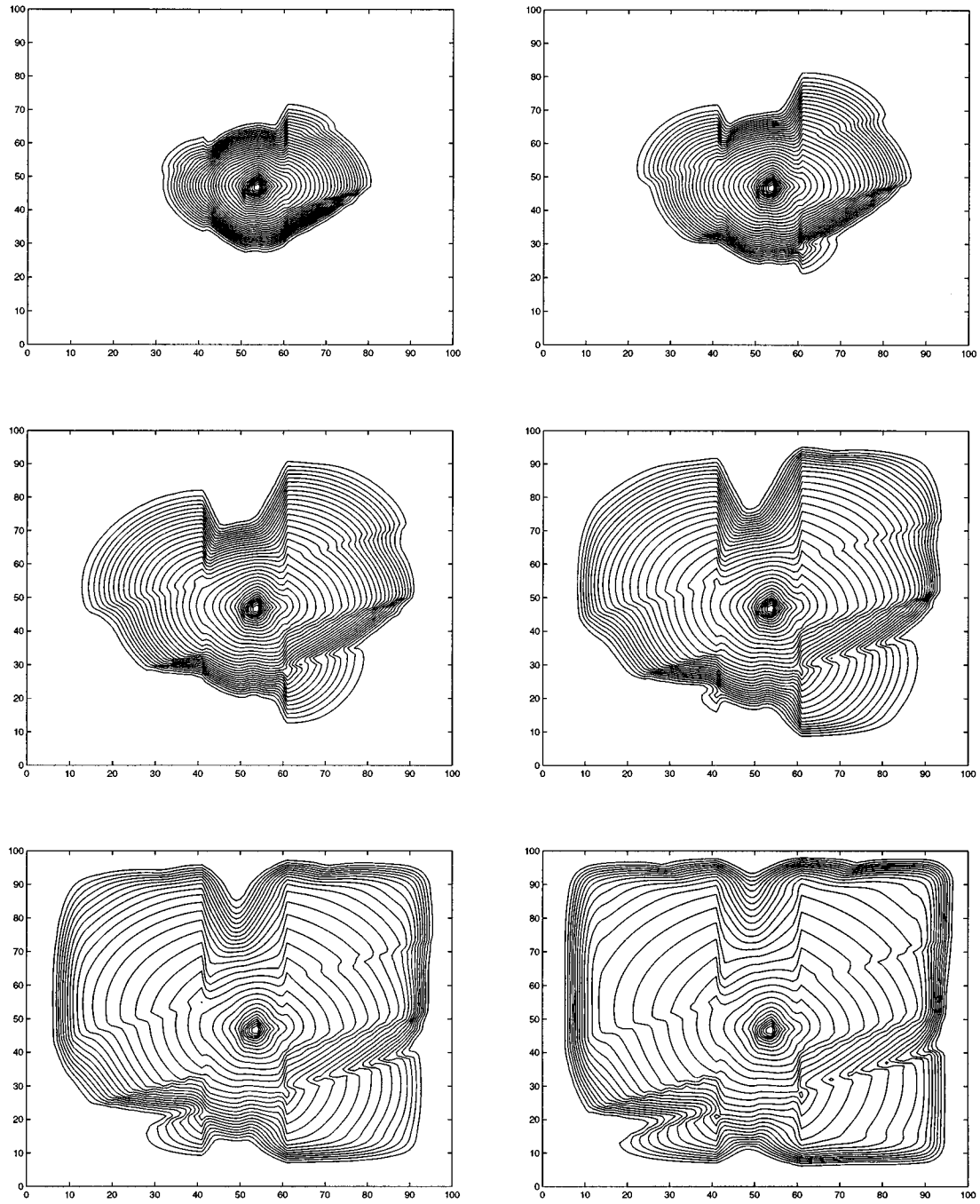

Fig. 11. Contour plot of the early time evolution of the electric field for the geometry depicted in Fig. 10.

size, chosen as $\Delta\rho = \Delta z = 0.02$ m. Moreover, because the diffusion mechanism is dominant, a stretching over the real part of the coordinates (i.e., a_z, a_ρ are chosen to be > 1) is indicated in the PML implementation. Therefore, we employ a ten-layer PML with quadractic profile for both its real and imaginary parts of ρ and z at the termination boundaries.

Fig. 11 illustrates the initial, early-time transient evolution as the pulse is launched into the formation through a series of snapshots of the field amplitude (contour plots) taken at the cross section of the formation, discretized by using a (N_ρ, N_ϕ, N_z) = (35, 70, 65) cylindrical grid. The different phase velocities and attenuation rates for the field are clearly visible. Moreover, the strong attenuation of the field as it reaches the PML layers near the boundaries of the grid is evident from the last two snapshots.

VI. Numerical Stability Considerations

Although both PML formulations furnish the same results in the previous examples, we have tested the codes for very long integration times and have observed discrepancies in their late time behaviors. This is illustrated in Fig. 11, which compares

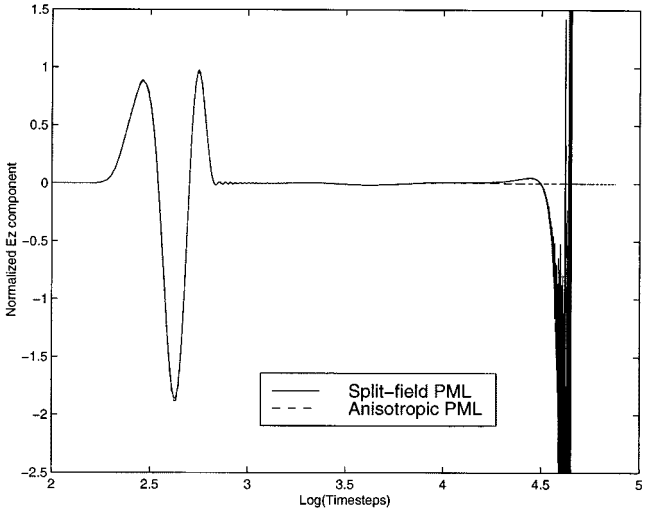

Fig. 12. Comparison between the late time behavior of the split-field PML (late-time unstable) and the unsplit field PML (stable). Note the logarithmic scale for the abscissa (time steps).

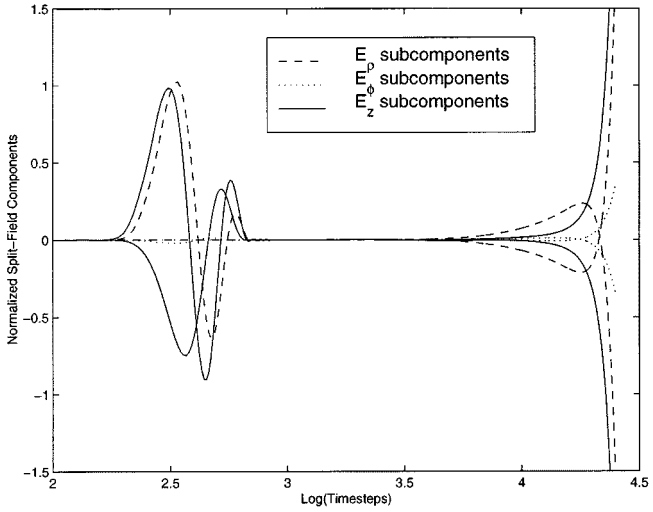

Fig. 13. Late time evolution of each split field subcomponent for the simulation in Fig. 12, now shown here separately. Note the logarithmic scale for the abscissa (time steps).

the late time behaviors of the two PML schemes. Note the logarithmic scale for the abscissa because of the very large number of time steps involved. This simulation uses a $(N_\rho, N_\phi, N_z) =$ (20, 30, 40) grid in free space, with a seven-cell PML in the ρ direction and ten-cell PML in the z direction. The source is an electric dipole at $(0.1N_\rho, 0.1N_\phi, 0.6N_z)$, and the receiver is at $(0.3N_\rho, 0.6N_\phi, 0.4N_z)$. The spatial discretization size is $\Delta_\rho = \Delta_z = 7.5$ cm, and the center frequency of the modified Blackman–Harris pulse is 200 MHz. In the case of the split-field formulation, the fields are split everywhere for a parallel implementation.

The results show that, while the unsplit PML is stable for such long integration times, the split-field is late time unstable. Since both schemes utilize the same spatial discretization, we rule out any inconsistency in the spatial discretization [48] as the cause of the instability. Rather, this phenomenon can be attributed to the weakly well posedness of the split-field system of equations, as discussed in [45]. There, it was shown that, while the unsplit scheme is strongly well posed (as the original Maxwell's system), the split-field equations are only weakly well posed. Moreover, although the total field in the split-field formulation (sum of the split components) coincide with the original unsplit EM fields, each of the nonphysical split fields (subcomponents) is unbounded, presenting secular terms with a linear growth in time which depends on their spatial derivatives. For very long integration times, this ultimately leads to very large values of the individual split fields, making a perfect cancellation of the total fields not possible anymore due to numerical roundoff effects. This ultimately causes a breakdown in the updates. This effect is more pronounced in schemes with high spatial resolution since the linear growth is higher for modes with large spatial frequency (at coarser resolutions, such modes are naturally cut off by the spatial discretization).

This is illustrated in Fig. 13. It depicts the evolution of each split field subcomponent of the previous simulation (note again the logarithmic scale for the abscissa). From this figure, we observe that, although the sum of the split field subcomponents leads to the correct total fields in the early time simulation, each split field ultimately grows unbounded and, at late times, perfect cancellation is not achieved anymore due to finite machine precision, leading to the instability phenomenon depicted in Fig. 12. The simulations were done in single precision.

Note that these observations refer to a split-field scheme where the fields are split everywhere, not only inside the PML ABC buffer region. This is highly desirable in parallel computations. The observed results are not necessarily present if the fields are split only in the PML region, where a strong loss mechanism is present. Also, it is important to point out that this observed phenomenon is perhaps only of theoretical interest. This is because, for practical applications, any result from the FDTD method at such very long integration times is of questionable utility anyway, since its accuracy is hampered by the accumulation of phase error due to numerical grid dispersion.

VII. Conclusions

FDTD schemes for the simulation of cylindrical geometries in inhomogeneous, dispersive, and conductive (lossy) media has been presented. The cylindrical PML ABC was extended to match the interior dispersive media for the outer radial boundary and to simulate open-space problems. Both the split-field and anisotropic versions of the PML were implemented and compared. The use of a PML is of particular interest for inhomogeneous, dispersive media since, in contrast to many previously employed ABC's, it can be implemented in a transparent manner with respect to the inhomogeneous and dispersive properties of the medium. In particular, multiterm dispersive models can be easily treated by combining the PML with the PLRC update scheme. Because the PML-PLRC-FDTD schemes presented here preserve the nearest-neighbor interaction property of the ordinary FDTD, they are also well suited for implementation on parallel machines.

REFERENCES

[1] L. B. Felsen, *Transient Electromagnetic Fields*. New York: Springer-Verlag, 1976.

[2] W. C. Chew, *Waves and Fields in Inhomogeneous Media*. Piscataway, NJ: IEEE Press, 1995.

[3] A. Taflove, *Computational Electromagnetics: The Finite Difference Time Domain Method*. Boston, MA: Artech House, 1995.

[4] R. Luebbers, F. P. Hunsgerger, K. S. Katz, R. B. Standler, and M. Schneider, "A frequency-dependent finite-difference time-domain formulation for dispersive materials," *IEEE Trans. Electromagn. Compat.*, vol. 32, pp. 222–227, 1990.

[5] D. Sullivan, "A frequency-dependent FDTD method for biological applications," *IEEE Trans. Microwave Theory Tech.*, vol. 40, pp. 532–539, Mar. 1992.

[6] ——, "Frequency-dependent FDTD methods using z transforms," *IEEE Trans. Antennas Propagat.*, vol. 40, pp. 1223–1230, Mar. 1992.

[7] C. M. Rappaport and W. H. Weedon, "Computational issues in ground penetrating radar," Center Electromagn. Res., Northeastern Univ., Boston, MA, 1994.

[8] ——, "A general method for FDTD modeling of wave propagation in arbitrary frequency dispersive materials," *IEEE Trans. Antennas Propagat.*, vol. 45, pp. 401–410, 1997.

[9] T. Kashiva, Y. Ohtomo, and I. Fukai, "A finite-difference time-domain formulation for transient propagation in dispersive media associated with Cole—Cole's circular arc law," *Microw. Opt. Technol. Lett.*, vol. 3, no. 12, pp. 416–419, 1990.

[10] R. M. Joseph, S. C. Hagness, and A. Taflove, "Direct time integration of Maxwell's equations in linear dispersive media with absorption for scattering and propagation of femtosecond electromagnetic pulses," *Opt. Lett.*, vol. 16, pp. 1412–1414, 1991.

[11] O. P. Gandhi, B.-Q. Gao, and J.-Y. Chen, "A frequency-dependent finite-difference time-domain formulation for general dispersive media," *IEEE Trans. Microwave Theory Tech.*, vol. 41, pp. 658–664, Apr. 1993.

[12] D. F. Kelley and R. J. Luebbers, "Piecewise linear recursive convolution for dispersive media using FDTD," *IEEE Trans. Antennas Propagat.*, vol. 44, pp. 792–797, June 1996.

[13] D. M. Sullivan, "Three dimensional optical fiber simulation," *Proc. 1997 IEEE Int. Symp. Antennas and Propagation*, vol. 1, pp. 368–371, 1997.

[14] J. R. Lovell and W. C. Chew, "Response of a point source in a multi-cylindrically layered medium," *IEEE Trans. Geosci. Remote Sensing*, vol. 25, pp. 850–858, Nov. 1987.

[15] A. Q. Howard and W. C. Chew, "Electromagnetic borehole fields in a layered, dipping-bed environment with invasion," *Geophysics*, vol. 57, no. 3, pp. 451–465, 1992.

[16] B. Anderson and W. C. Chew, "Transient response of some borehole mandrel tools," *Geophysics*, vol. 54, no. 2, pp. 216–224, 1989.

[17] Q. H. Liu, "Electromagnetic field generated by an off-axis source in a cylindrically layered medium with an arbitrary number of horizontal discontinuities," *Geophysics*, vol. 58, no. 5, pp. 616–625, 1993.

[18] C. Olson and D. G. Hall, "Radiation patterns of higher order azimuthal order spatial modes from a concentric-circle-grating waveguide cavity using the volume-current method," *IEEE J. Quantum Electron.*, vol. 34, pp. 2298–2307, Dec. 1998.

[19] W. C. Chew and Q. H. Liu, "Inversion of induction tool measurements using the distorted Born iterative method and CG-FFHT," *IEEE Trans. Geosci. Remote Sensing*, vol. 32, pp. 878–884, July 1994.

[20] H. Wenzel and H. J. Wuensche, "Effective frequency method in the analysis of vertical-cavity surface-emitting lasers," *IEEE J. Quantum Electron.*, vol. 33, pp. 1156–1162, July 1997.

[21] R. R. Burton, M. S. Stern, P. C. Kendall, and P. N. Robson, "VCSEL diffraction-loss theory," *Proc. Inst. Elect. Eng. Optoelectronics*, vol. 142, no. 2, pp. 77–81, 1995.

[22] M. Fusco, "FDTD algorithm in curvilinear coordinates," *IEEE Trans. Antennas Propagat.*, vol. 38, pp. 76–89, Jan. 1990.

[23] M. Mrozowski, M. Okoniewski, and M. A. Stuchly, "Hybrid PEE-FDTD method for efficient field modeling in cylindrical coordinates," *Electron. Lett.*, vol. 32, no. 3, pp. 194–195, 1996.

[24] J.-Q. He and Q. H. Liu, "A nonuniform cylindrical FDTD algorithm with improved PML and quasi-PML absorbing boundary conditions," *IEEE Trans. Geosci. Remote Sensing*, vol. 37, pp. 1066–1072, Mar. 1999.

[25] Y. Chen and R. Mittra, "A highly efficient finite-difference time domain algorithm for analyzing axisymmetric waveguides," *Microw. Opt. Technol. Lett.*, vol. 15, no. 4, pp. 201–203, 1997.

[26] Q. H. Liu, "A PSTD algorithm in cylindrical coordinates," in *Proc. Annu. Rev. Progress in Applied Computational Electromagnetics*, vol. 2, Monterey, CA, Mar. 16–20, 1998, pp. 845–851.

[27] J. Berenger, "Three-dimensional perfectly matched layer for the absorption of electromagnetic waves," *J. Comput. Phys.*, vol. 127, no. 2, pp. 363–379, 1996.

[28] W. C. Chew and W. Weedon, "A 3-D perfectly matched medium from modified Maxwell's equations with stretched coordinates," *Microw. Opt. Technol. Lett.*, vol. 7, no. 13, pp. 599–604, 1994.

[29] D. S. Katz, E. T. Thiele, and A. Taflove, "Validation and extension to three dimensions of the Berenger PML absorbing boundary condition," *IEEE Microwave Guided Wave Lett.*, vol. 4, pp. 268–270, Aug. 1994.

[30] C. M. Rappaport, "Interpreting and improving the PML absorbing boundary condition using anisotropic lossy mapping of space," *IEEE Trans. Magn.*, vol. 32, pp. 968–974, May 1996.

[31] Z. S. Sacks, D. M. Kingsland, R. Lee, and J.-F. Lee, "A perfectly matched anisotropic absorber for use as an absorbing boundary condition," *IEEE Trans. Antennas Propagat.*, vol. 43, pp. 1460–1463, Dec. 1995.

[32] S. D. Gedney, "An anisotropic PML absorbing media for the FDTD simulation of fields in lossy and dispersive media," *Electromagn.*, vol. 16, pp. 399–415, 1996.

[33] L. Zhao and A. C. Cangellaris, "GT-PML: The generalized theory of perfectly matched layers and its application to the reflectionless truncation of finite-difference time-domain grids," *IEEE Trans. Microwave Theory Tech.*, vol. 44, pp. 2555–2563, Dec. 1996.

[34] Y. H. Chen, W. C. Chew, and M. L. Oristaglio, "Application of perfectly matched layers to the transient modeling of subsurface EM problems," *Geophysics*, vol. 62, no. 6, pp. 1730–1736, 1997.

[35] F. Collino and P. Monk, "The perfectly matched layer in curvilinear coordinates," *SIAM J. Sci. Computing*, vol. 19, pp. 2061–2090, 1998.

[36] W. C. Chew, J. M. Jin, and E. Michielssen, "Complex coordinate system as a generalized absorbing boundary condition," in *Proc. 13th Annu. Rev. Progress of Applied Computational Eletromagnetics*, vol. 2, Monterey, CA, Mar. 17–21, 1997, pp. 909–914.

[37] J. Maloney, M. Kesler, and G. Smith, "Generalization of PML to cylindrical geometries," in *Proc. 13th Annu. Rev. Programming of Applied Computer Eletromagnetics*, vol. 2, Monterey, CA, Mar. 17–21, 1997, pp. 900–908.

[38] F. L. Teixeira and W. C. Chew, "PML-FDTD in cylindrical and spherical grids," *IEEE Microwave Guided Wave Lett.*, vol. 7, pp. 285–287, Sept. 1997.

[39] ——, "Systematic derivation of anisotropic PML absorbing media in cylindrical and spherical coordinates," *IEEE Microwave Guided Wave Lett.*, vol. 7, pp. 371–373, Nov. 1997.

[40] ——, "Analytical derivation of a conformal perfectly matched absorber for electromagnetic waves," *Microwave Opt. Technol. Lett.*, vol. 17, pp. 231–236, 1998.

[41] F. Collino and P. Monk, "Optimizing the perfectly matched layer," , to be published.

[42] F. L. Teixeira and W. C. Chew, "General closed-from PML constitutive tensors to match arbitrary bianisotropic and dispersive linear media," *IEEE Microwave Guided Wave Lett.*, vol. 8, pp. 223–225, June 1998.

[43] F. L. Teixeira, W. C. Chew, M. Straka, M. L. Oristaglio, and T. Wang, "Finite-difference time-domain simulation of ground penetrating radar on dispersive, inhomogeneous, and conductive soils," *IEEE Trans. Geosci. Remote Sensing*, vol. 36, pp. 1928–1937, June 1998.

[44] G.-X. Fan and Q. H. Liu, "A PML-FDTD algorithm for general dispersive media," in *Proc. 14th Annu. Rev. Progress Applied Computational Eletromagnetics*, Monterey, CA, Mar. 16–20, 1998, pp. 655–662.

[45] S. Abarbanel and D. Gottlieb, "A mathematical analysis of the PML method," *J. Comput. Phys.*, vol. 134, pp. 357–363, 1997.

[46] J. N. Brittingham, E. K. Miller, and J. L. Wilows, "Pole-extraction from real frequency information," *Proc. IEEE*, vol. 68, pp. 263–273, 1980.

[47] F. L. Teixeira and W. C. Chew, "Differential forms, metrics, and the reflectionless absorption of electromagnetic waves," *J. Electromagn. Waves Appl.*, vol. 13, pp. 665–686, 1999.

[48] ——, "Lattice electromagnetic theory from a topological viewpoint," *J. Math. Phys.*, vol. 40, no. 1, pp. 169–187, 1999.

[49] I. J. Craddock, C. J. Railton, and J. P. McGeehan, "Derivation and application of a passive equivalent circuit for the finite difference time domain algorithm," *IEEE Microwave Guided Wave Lett.*, vol. 6, pp. 40–42, Jan. 1996.

[50] K. M. Krishnaiah and C. J. Railton, "Passive equivalent circuit of FDTD: An application to subgridding," *Electron. Lett.*, vol. 33, pp. 1277–1278, 1997.

[51] P. Thoma and T. Weiland, "A consistent subgridding scheme for the finite difference time domain method," *Int. J. Numer. Model.*, vol. 9, pp. 359–374, 1996.

[52] J. E. Hipp, " Soil electromagnetic parameters as functions of frequency, soil density, and soil moisture," *Proc. IEEE*, vol. 62, pp. 98–103, 1974.

[53] W. C. Chew and J. M. Jin, "Perfectly matched layers in discretized space: An analysis and optimization," *Electromagnetics*, vol. 16, pp. 325–340, 1996.
[54] T. G. Moore, J. G. Blaschak, A. Taflove, and G. A. Kriegsmann, "Theory and application of radiation boundary operators," *IEEE Trans. Antennas Propagat.*, vol. 36, pp. 1797–1812, Dec. 1988.
[55] C. Liu and L. C. Chen, "Numerical simulation of subsurface radar for detecting buried pipes," *IEEE Trans. Geosci. Remote Sensing*, vol. 29, pp. 795–798, July 1991.
[56] M. Moghaddam, W. C. Chew, B. Anderson, E. Yannakis, and Q. H. Liu, "Computation of transient electromagnetic waves in inhomogeneous media," *Radio Sci.*, vol. 26, pp. 265–273, Jan. 1991.
[57] M. Moghaddam, E. J. Yannakakis, W. C. Chew, and C. Randall, "Modeling of the subsurface interface radar," *J. Electromagn. Waves Appl.*, vol. 5, pp. 17–39, 1991.
[58] Y. He, T. Uno, S. Adachi, and T. Mashiko, "Two-dimensional active imaging of conducting objects buried on a dielectric half-space," *IEICE Trans. Commun.*, vol. E76-B, no. 12, pp. 1546–1551, 1993.
[59] K. Demarest, R. Plumb, and Z. Huang, "The performance of FDTD absorbing boundary conditions for buried scatterers," in *Proc. URSI Radio Science Meeting*, 1994, p. 169.
[60] B. J. Hook, "FDTD modeling of ground-penetrating radar antennas," in *Proc. 11th Annu. Rev. Progress of Applied Computational Eletromagnetics*, Monterey, CA, 1995, pp. 740–747.
[61] J. M. Bourgeois and G. S. Smith, "A fully three-dimensional simulation of a ground-penetrating radar: FDTD theory compared with experiment," *IEEE Trans. Geosci. Remote Sensing*, vol. 34, pp. 36–44, Jan. 1996.
[62] J. Calhoun, "A finite difference time domain (FDTD) simulation of electromagnetic wave propagation and scattering in a partially conducting layered earth," in *Proc. 1997 IGARSS: Int. Geoscience and Remote Sensing Symp.*, Singapore, 1997, pp. 922–924.
[63] G. A. Newman and D. L. Alumbaugh, "3-D electromagnetic modeling using staggered finite differences," in *Proc. 1997 IGARSS: Int. Geoscience and Remote Sensing Symp.*, Singapore, 1997, pp. 929–931.
[64] S. Agosti, G. G. Gentili, and U. Spagnolini, "Electromagnetic inversion of monostatic GPR: Application to pavement profiling," in *Proc. 1997 Int. Conf. Electromagnetic Advanced Applications (ICEAA'97)*, Torino, Italy, 1997, pp. 491–494.
[65] W. C. Chew, "Modeling of the dielectric logging tool at high frequencies: Theory," *IEEE Trans. Geosci. Remote Sensing*, vol. 26, pp. 382–387, July 1988.
[66] ——, "Modeling of the dielectric logging tool at high frequencies: Application and results," *IEEE Trans. Geosci. Remote Sensing*, vol. 26, pp. 388–398, July 1988.

Fernando L. Teixeira received the B.S. and M.S. degrees from the Pontifical Catholic University (PUC-Rio), Rio de Janeiro, Brazil, in 1991 and 1995, respectively, and the Ph.D. from the University of Illinois, Urbana, in 1999, all in electrical engineering.

From 1992 to 1994, he was a Technical Officer with the Military Institute of Engineering (IME) and the Brazilian Army R&D Center (IPD-CTEx), Rio de Janeiro. From 1994 to 1996, he was a Member of the Technical Staff, Satellite Transmission Department, EMBRATEL S.A. (MCI/Worldcom), Rio de Janeiro. From 1996 to 1999, he was a Research and Teaching Assistant with the Center for Computational Electromagnetics, University of Illinois. Since 1999, he has been a Postdoctoral Associate with the Research Laboratory of Electronics, Massachusetts Institute of Technology (MIT), Cambridge, MA. His current research interests include wave propagation and scattering modeling for communication, sensing, and device applications. His previous research include analysis and synthesis of reflector antennas, surface interpolation techniques, and simulation of lattice gauge theories. He has co-authored more than 40 refereed papers in those areas.

Dr. Teixeira is a member of Phi Kappa Phi. He was a recipient of a CAPES/Brasilia Fellowship (1996–1999), a 1998 IEEE MTT-S Graduate Fellowship Award, the 1999 Raj Mittra Outstanding Research Award from the University of Illinois, and has won paper awards at the 1999 USNC/URSI Meeting, Boulder, CO, and the 1999 IEEE AP-S International Symposium, Orlando, FL.

Weng Cho Chew (M'79–SM'86–F'93) received the B.S. degree in 1976, both the M.S. and Engineer's degrees in 1978, and the Ph.D. degree in 1980, all in electrical engineering, from the Massachusetts Institute of Technology (MIT), Cambridge.

From 1981 to 1985, he was with Schlumberger–Doll Research, Ridgefield, CT, where he was Program Leader and later Department Manager. From 1985 to 1990, he was an Associate Professor with the Department of Electrical and Computer Engineering, University of Illinois, Urbana, where he is currently a Professor and teaches graduate courses in waves and fields in inhomogeneous media and theory of microwave and optical waveguides and supervises a graduate research program. From 1989 to 1993, he was the Associate Director of the Advanced Construction Technology Center, University of Illinois. Presently, he is the Director of the Center for Computational Electromagnetics and the Electromagnetics Laboratory. His name is listed many times in the *List of Excellent Instructors* on campus. He authored the book *Waves and Fields in Inhomogeneous Media*, published over 200 scientific journal articles, and presented over 270 conference papers. His recent research interest has been in the area of wave propagation, scattering, inverse scattering, and fast algorithms related to scattering, inhomogeneous media for geophysical subsurface sensing and nondestructive testing applications. Previously, he analyzed electrochemical effects and dielectric properties of composite materials, microwave and optical waveguides, and microstrip antennas. Since 1996 he has been an Associate Editor of the *Journal of Electromagnetic Waves and Applications* and *Microwave Optical Technology Letters*. He was also an Associate Editor for the *International Journal of Imaging Systems and Technology* from 1989 to 1994, and was a Guest Editor of *Radio Science* in 1986, *International Journal of Imaging Systems and Technology* in 1989, and *Electromagnetics* in 1995.

Dr. Chew is a member of Eta Kappa Nu, Tau Beta Pi, URSI Commisions B and F, and is an active member of the Society of Exploration Geophysics (SEG). He was a National Science Foundation (NSF) Presidential Young Investigator for 1986 and an AdCom member of the IEEE Geoscience and Remote Sensing Society. Since 1984, he has been an Associate Editor of the IEEE TRANSACTIONS ON GEOSCIENCE AND REMOTE SENSING. He is the recipient of the 2000 IEEE Graduate Teaching Award and a Distinguished Founder Professorship from the College of Engineering, University of Illinois.